

Electromagnetic effects on charged particles in a near-horizon-extreme-Kerr geometry

Yehui Hou,¹ Zhenyu Zhang¹,,¹ Minyong Guo^{2,*},^{2,*} and Bin Chen^{1,3,4}

¹*Department of Physics, Peking University, No.5 Yiheyuan Road, Beijing 100871, People's Republic of China*

²*Department of Physics, Beijing Normal University, Beijing 100875, People's Republic of China*

³*Center for High Energy Physics, Peking University, No. 5 Yiheyuan Road, Beijing 100871, People's Republic of China*

⁴*Collaborative Innovation Center of Quantum Matter, No. 5 Yiheyuan Road, Beijing 100871, People's Republic of China*



(Received 31 January 2023; accepted 25 May 2023; published 9 June 2023)

We investigate the motions of charged particles in the near horizon region of an extreme Kerr black hole with weak electromagnetic fields. There is an enhanced symmetry in the near-horizon-extreme-Kerr geometry. We find that when the electromagnetic field respects this enhanced symmetry, which we refer to as the maximally symmetric electromagnetic field, the equations of motion of charged particles get simplified into a set of decoupled first-order differential equations. We discuss the motions of charged particles in two maximally symmetric electromagnetic fields, one being the force-free field and the other being the vacuum fields. Even though the radial motions are similar to the geodesics in near-horizon-extreme-Kerr geometry, the angular motions could be affected by the electromagnetic field significantly. In particular, for the vacuum solution that is produced by a weakly charged black hole, there exist stable vortical motions if the electromagnetic parameter is above the critical value $\mathfrak{B}_c = \sqrt{3}$. These vortical motions do not cross the equatorial planes, and the charged particles in them radiate nonthermally. We discuss the corresponding astrophysical implications.

DOI: [10.1103/PhysRevD.107.124014](https://doi.org/10.1103/PhysRevD.107.124014)

I. INTRODUCTION

Black holes are astronomical objects of great interests. In recent years, the horizon-scale images of supermassive black holes released by Event Horizon Telescope (EHT) collaborations [1,2] have pushed the study of black hole physics in strong gravity regime to a new level. By comparing the observational data with theoretical models, they allow us to estimate the masses and spins of black holes, draw the magnetic field configurations around the black holes and investigate the physics in the accretion disks.

The (electro)magnetic field around a black hole affect significantly the images of the black hole. It not only changes the worldlines of charged particles from the geodesics to more general trajectories, but also induces the synchrotron radiation. The Lorentz force significantly affects the motions of electrons and ions, which triggers a series of observable phenomena such as the jets, the synchrotron radiation, and the gamma-ray bursts [3]. The polarized images of black holes encode rich information on

the structure of the electromagnetic fields and the dynamics of charged particles [4–11]. The electromagnetic fields surrounding the astronomical black holes [12–14] are widely believed to originate from the accreted plasma, even though there are also discussions about the possibility that the black hole charge act as the source of electromagnetic fields [15,16]. In any case, there are new configurations of classical electrodynamics fields in the curved spacetime, which do not exist in a flat spacetime, and the motions of the charged particles in them present novel features.

For geometrically thin accretion disks, the fluid motion can be approximated at the lowest order as single-particle trajectories on the equatorial plane. The problem of the fluid motion effectively reduces to an analysis of the effective radial potential of a single charged particle [17–23]. Moreover, richer physical processes exist in the off-equatorial region governed by the magnetosphere of black holes. In this region, the single-particle approximation of the dilute plasma works even better [15]. For integrable systems like the Reissner-Nordström and Kerr-Newman black holes, the charged particle motions are regular [24–26] and behave as continuous lines on the Poincaré section. However, the electromagnetic fields

*Corresponding author.
minyongguo@bnu.edu.cn

generically destroy the integrability, making the analytical study of the off-equatorial motions impossible. One has to employ the numerical methods and carefully select the initial conditions. More related works can be found in [27–30]. In addition, the nonintegrability generally leads to chaotic motions of the particles as the scattered dots on the Poincare section [31–35]. However, if the spacetime is highly symmetric, and for special electromagnetic field configuration, the off-equatorial motions of charged particles can still be studied analytically, which allow us to gain more insights of the physics.

It is well known that the near-horizon-extreme-Kerr (NHEK) geometry has an enhanced symmetry, which has led to extensive theoretical studies [36–43]. Based on observational evidences of high-spin black holes [44,45], there is a variety of analytical studies on the possible astronomical observation [46–59]. Among them, the force-free electrodynamics in NHEK were studied in [48–51], and the extreme Kerr accretion was investigated in [46,53]. In [47], the authors studied the motions of charged particles under the Wald potential in the NHEK geometry. They found that the motions can be solved analytically, and they investigated the motions in the equatorial plane and along the spin axis. However, the electromagnetic effects on the off-equatorial motions of the charged particles in the extreme Kerr spacetime has not been explored much.

In this work, we study the motions of charged particles in the NHEK geometry, in the presence of weak electromagnetic fields. We neglect the backreaction effect to the spacetime, as the electromagnetic field is weak. We find that under maximally symmetric electromagnetic (MSEM) fields, the Carter constant is geometrically realized by the symmetry of the system. Thus, we are allowed to have an analytical study of the motion of charged particles. We derive the first-order differential equations of motion of charged particles for universal MSEM fields and discuss some general properties of the angular potential. Then we consider two kinds of MSEM fields, the force-free one and a general vacuum field, and study the motion of charged particles in them. In particular, the vacuum field with the Z_2 symmetry under $\theta \rightarrow \pi - \theta$ is exactly the Wald solution [60] in the near-horizon limit, which describes an electromagnetic field generated by a weakly charged black hole. We present a complete analysis of the charged particle motions in the Wald solution, and especially have a detailed discussion on the vortical motions.

The paper is organized as follows. In Sec. II, we shall first review the NHEK geometry and its isometric group. In Sec. III, we derive the first-order differential equations of motion of charged particle motion under MSEM fields. The fields do not affect the radial motion, and we briefly discuss its classification. In Sec. IV, the angular motions under different types of MSEM fields are explored. We summarize and conclude this work in Sec. V. We work in the geometrized unit with $G = c = 1$ in this paper.

II. EXTREME KERR BLACK HOLES

A. NHEK limit

The Kerr geometry is a generally accepted description of astrophysical black holes within the framework of Einstein’s gravity. In Boyer-Lindquist coordinates, the metric is given by

$$ds^2 = -\frac{\Delta}{\Sigma}(d\tilde{t} - a \sin^2\tilde{\theta}d\tilde{\phi})^2 + \Sigma\left(\frac{d\tilde{r}^2}{\Delta} + d\tilde{\phi}^2\right) + \frac{\sin^2\tilde{\theta}}{\Sigma}[a d\tilde{t} - (\tilde{r}^2 + a^2)d\tilde{\phi}]^2, \quad (2.1)$$

where

$$\Sigma(\tilde{r}, \tilde{\theta}) = \tilde{r}^2 + a^2 \cos^2\tilde{\theta}, \quad \Delta(\tilde{r}) = \tilde{r}^2 - 2M\tilde{r} + a^2. \quad (2.2)$$

The parameter M is the mass of the black hole, $a = J/M$ denotes the spin parameter, with J the angular momentum of the black hole. The metric is invariant under $a \rightarrow -a$, $\phi \rightarrow -\phi$, so we can set $a \geq 0$ for simplicity and without loss of generality. The coordinate singularities are located at $\tilde{r}_{\pm} = M \pm \sqrt{M^2 - a^2}$, and \tilde{r}_+ is the radius of the event horizon. To avoid naked singularities, $a \leq M$ has to be satisfied. When $a \rightarrow M$, one has an extreme Kerr black hole, whose near-horizon geometry is very different from the usual Kerr spacetime. In this case, one can use the method developed by Bardeen and Horowitz [36] to obtain the near-horizon geometry. Consider a small deviation from the extremality

$$a = M\sqrt{1 - \epsilon^2}, \quad (2.3)$$

where $\epsilon \ll 1$ is a small factor. Then we perform a dilation onto the horizon

$$t = \frac{\epsilon^p}{2M}\tilde{t}, \quad r = \frac{\tilde{r} - M}{\epsilon^p M}, \quad \theta = \tilde{\theta}, \quad \phi = \tilde{\phi} - \frac{\tilde{t}}{2M}, \quad (2.4)$$

with $0 < p \leq 1$ being the “zoom power.” Different p will zoom into different near-horizon regions (e.g., the ISCO is in $p = 2/3$), and the proper distance is proportional to $|\log \epsilon|$ [40]. For each $p < 1$, expanding the metric to the leading order of ϵ , we can get the NHEK geometry

$$ds^2 = 2M^2\Gamma\left[-r^2 dt^2 + \frac{dr^2}{r^2} + d\theta^2 + \Lambda^2(d\phi + rdt)^2\right] + \mathcal{O}(\epsilon), \quad (2.5)$$

$$\Gamma = \frac{1 + \cos^2\theta}{2}, \quad \Lambda = \frac{2 \sin \theta}{1 + \cos^2\theta}. \quad (2.6)$$

It is worth emphasizing that the NHEK geometry is an exact solution to the vacuum Einstein equations and

describes the near-horizon region of the extreme Kerr black hole through the coordinate rescaling Eq. (2.4). However, it is not asymptotically flat. For a fixed θ , the NHEK geometry is a $U(1)$ -fibered AdS_2 , in which the geometry along the spin axis is exactly AdS_2 . For $p = 1$, the expansion gives the near-NHEK geometry at the leading order, which takes the form

$$ds^2 = 2M^2\Gamma \left[-(r^2 - 1)dt^2 + \frac{dr^2}{r^2 - 1} + d\theta^2 + \Lambda^2(d\phi + rdt)^2 \right] + \mathcal{O}(\epsilon). \quad (2.7)$$

Since p corresponds to the extent of zooming, near-NHEK is the deepest region where the horizon is located. The other $p < 1$ corresponds to the regions with different depths, which are all described by the NHEK. As pointed out in [38], Eqs. (2.7) and (2.5) are locally diffeomorphic to each other, under a coordinate transformation not involving the θ direction. On the other hand, as shown in Sec. III A, the electromagnetic field does not change the radial motion of the particles. Thus we only discuss physical processes in the NHEK geometry without loss of generality. From now on, we set $M = 1$ for simplicity.

B. The isometry group

Different from stationary and axisymmetric Kerr spacetime (2.1), which has two Killing vectors $\partial_t, \partial_\phi$, the NHEK geometry possesses an enhanced Killing symmetry. At an infinitesimal level, the isometry group is generated by

$$\begin{aligned} W &= \partial_\phi, & H_0 &= t\partial_t - r\partial_r, \\ H_+ &= \partial_t, & H_- &= \left(t^2 + \frac{1}{r^2}\right)\partial_t - 2tr\partial_r - \frac{2}{r}\partial_\phi. \end{aligned} \quad (2.8)$$

The Killing vectors W and H_+ are the translations along the ϕ direction and t direction, respectively, and H_0 implies a self-similarity under the scaling $t \rightarrow t/\lambda, r \rightarrow \lambda r$. The fourth Killing vector H_- denotes the time translational invariance when transforming to the global coordinates (an analog) of AdS_2 [36]. The commutation relations between the generators are

$$[H_0, H_\pm] = \mp H_\pm, \quad [H_+, H_-] = 2H_0, \quad [W, H_{\pm,0}] = 0, \quad (2.9)$$

which generate a $\text{SL}(2, \mathbb{R}) \times \text{U}(1)$ isometry group. Simply speaking, the $\text{SL}(2, \mathbb{R})$ subgroup is the isometry of AdS_2 , while $\text{U}(1)$ is the translational group along ϕ . The quadratic Casimir is

$$C^{\mu\nu} = -H_0^\mu H_0^\nu + \frac{1}{2}(H_+^\mu H_-^\nu + H_-^\mu H_+^\nu). \quad (2.10)$$

Recall that the Kerr spacetime has an irreducible Killing tensor, $K^{\mu\nu}$, which generally cannot be constructed using any Killing vectors. Thus, the Killing tensor implies a nongeometrically realized symmetry and a Carter constant of motion along geodesics, $K = K^{\mu\nu} p_\mu p_\nu$. As a result, r and θ in the Hamilton-Jacobi equation can be separated [24]. For an extreme Kerr black hole, when zooming into NEHK, $K^{\mu\nu}$ becomes reducible

$$K^{\mu\nu} = g^{\mu\nu} + W^\mu W^\nu + C^{\mu\nu}, \quad (2.11)$$

where $g^{\mu\nu}$ is the metric component. Therefore, due to the enhanced Killing symmetry in NHEK, $K^{\mu\nu}$ can be constructed by the Killing vectors, and the Carter constant is geometrically realized by the Casimir. This property will help us to obtain the equations of motion in NHEK with electromagnetic fields.

III. PARTICLE DYNAMICS IN A MSEM FIELD

In this section, we study the dynamics of charged particles in NHEK with a weak electromagnetic field, whose backreaction to the spacetime can be neglected. Despite the Lorentz force, the Killing symmetries can still be used to construct conserved quantities along the trajectories in the presence of a MSEM field, whose Lie derivatives along the Killing vector fields of NHEK are vanishing. Consequently, we may obtain the first-order differential equations of motion of charged particles.

A. The equations of motion

If the specific charge is large enough, then the Lorentz force can be rather strong compared to the gravitation. For electrons, even a magnetic field of 1 Gauss around a black hole of solar mass can produce an Lorentz force of nearly 100 times the magnitude of the gravitation. For a particle of charge q and mass m , neglecting the radiation-reaction force, its equation of motion reads

$$D_\tau U^a = \frac{q}{m} F^{ab} U_b, \quad (3.1)$$

where U^a and F^{ab} are the four velocity and electromagnetic field strength tensor, respectively, and D_τ is the covariant derivative about the proper time τ . If the electromagnetic field is invariant along a Killing vector ξ , i.e.,

$$\mathcal{L}_\xi \mathcal{A} = [\xi, \mathcal{A}] = 0, \quad (3.2)$$

where \mathcal{A} is the electromagnetic field potential, \mathcal{L}_ξ is the Lie derivative along ξ , then we have

$$D_\tau(\xi_\mu P^\mu) = qU^\nu (\mathcal{L}_\xi \mathcal{A})_\nu = 0. \quad (3.3)$$

Here $P^\mu = mU^\mu + qA^\mu$ denotes the canonical momentum. Even though one can define the energy and angular

momentum of a charged particle in a stationary and axisymmetric spacetime, one has to evolve the second-order differential equations of motion numerically [31,34] since the Carter constant gets lost. However, in NHEK, the geometric symmetry of the electromagnetic field can be enhanced in such a way that the dynamics of the charged particles could be simplified. More precisely, if the electromagnetic field is maximally symmetric, then it has a $\text{SL}(2, \mathbb{R}) \times \text{U}(1)$ invariant potential satisfying

$$\mathcal{L}_W \mathcal{A} = 0, \quad \mathcal{L}_{H_0} \mathcal{A} = 0, \quad \mathcal{L}_{H_\pm} \mathcal{A} = 0, \quad (3.4)$$

and there are four constants of motion,

$$\begin{aligned} E &= -H_+^\mu P_\mu = -P_t, & L &= W^\mu P_\mu = P_\phi, \\ h_0 &= H_0^\mu P_\mu = -Et - rP_r, \\ h_- &= H_-^\mu P_\mu = -\left(t^2 + \frac{1}{r^2}\right)E - 2trP_r - \frac{2}{r}L. \end{aligned} \quad (3.5)$$

The constants E and L are the NHEK analogs of the energy and angular momentum.¹ The constant h_0 originates from the self-similarity of the system under $t \rightarrow t/\lambda, r \rightarrow \lambda r$, and h_- is from the translational invariance along the global time. An important property is that, under an MSEM field, the Carter constant is restored

$$C = C^{\mu\nu} P_\mu P_\nu = -h_0^2 - Eh_-, \quad (3.6)$$

which implies the separability of the Hamilton-Jacobi equation. To see this, we need the specific form of the MSEM field. Denote the potential as \mathcal{A}_{MS} , in the gauge $A_\theta = 0$, the 1-form potential satisfying Eq. (3.4) must be of the form

$$\mathcal{A}_{\text{MS}} = f(\theta)(d\phi + rdt), \quad (3.7)$$

where $f(\theta)$ is an undetermined function of θ . We may transform the 1-form potential into a vector potential with only one nonvanishing component

$$A^\phi = \frac{f(\theta)}{2\Gamma\Lambda^2}. \quad (3.8)$$

In other words, the vector potential \mathcal{A}_{MS} is proportional to W , such that it is obviously invariant under the isometry group. Within the gauge we have chosen, C directly gives a first-order differential equation,

¹By the rescaling Eq. (2.4) we have $\tilde{E} = \epsilon E/2 + L/2, \tilde{L} = L$, where the tilde denotes the quantities in the Kerr spacetime. Thus, when moving in the NHEK region, the particle's Kerr energy is determined by L if neglecting the $\mathcal{O}(\epsilon)$ correction. Note that only particles with $L > 2m$ can reach the infinity.

$$C = -r^2 U_r^2 + \frac{E^2}{r^2} + \frac{2EL}{r}, \quad (3.9)$$

where and hereafter E, L are rescaled by $1/m$, and C rescaled by $1/m^2$, thus all the conserved quantities become dimensionless. Combining Eq. (3.9) with $U^a U_a = -1$, we can get rid of the U_r component and find a first-order differential equation of the polar angle,

$$C = U_\theta^2 + \left(\frac{1}{\Lambda^2} - 1\right)L^2 + 2\Gamma + \frac{k^2 f^2(\theta) - 2kL f(\theta)}{\Lambda^2}, \quad (3.10)$$

where $k = q/m$ denotes the specific charge. As a result, the equations are separated, and the trajectories are regular. Our result is consistent with [31], where the authors used numerical methods to study the trajectories in the Kerr spacetime and found that almost all trajectories become regular in the limit $a \rightarrow M$. For convenience, we rewrite the equations of motion in the following forms

$$2\Gamma \frac{dt}{d\tau} = \frac{E + Lr}{r^2}, \quad (3.11)$$

$$2\Gamma \frac{d\phi}{d\tau} = \frac{L}{\Lambda^2} - \frac{E + Lr}{r} - k \frac{f(\theta)}{\Lambda^2}, \quad (3.12)$$

$$2\Gamma \frac{dr}{d\tau} = \pm_r \sqrt{R(r)}, \quad (3.13)$$

$$2\Gamma \frac{d\theta}{d\tau} = \pm_\theta \sqrt{\Theta(\theta)}. \quad (3.14)$$

Here the symbols \pm_r, \pm_θ denote the sign of U^r and U^θ , respectively, and we have introduced the radial and angular potentials

$$R(r) = -Cr^2 + 2ELr + E^2, \quad (3.15)$$

$$\Theta(\theta) = C + L^2 - 2\Gamma - \frac{1}{\Lambda^2} [L - kf(\theta)]^2. \quad (3.16)$$

The potentials must be non-negative along the trajectories. Note that only the angular potential Eq. (3.16) gets changed by the presence of MSEM field, compared with the ones without electromagnetic field. This is one of the main results in this work. One can see that when the specific charge $k = 0$, Eq. (3.16) reduces to the form for geodesics in NHEK. However, since $f(\theta)$ is an undetermined function that depends on the choice of the potential \mathcal{A}_{MS} , we need to carefully analyze the angular potential based on different electromagnetic field configurations. Moreover, as k increases, the conserved quantities L and C also increase, and the term “ 2Γ ” in Eq. (3.16) becomes negligible. Nevertheless, we will focus on the general case and retain the “ 2Γ ” term in our discussion.

In addition, although the MSEM field also affects the motion of ϕ , the effect is somehow trivial. In fact, from Eq. (2.4), we learn that $d\tilde{\phi} = d\phi + dt/\epsilon \sim dt/\epsilon$, which means ϕ always increases for the future-directed particles.

B. The classification of radial motions

As the radial potential keeps invariant, the classification of the motions of charged particles in the r direction is the same as the ones of the geodesics in NHEK, which has been discussed in [40,41]. We give a brief review here. At first, since t is the global time in NHEK, a future-directed trajectory should satisfy $dt/dr > 0$, which gives

$$r \geq r_c = -\frac{E}{L}, \quad \text{if } L \geq 0, \quad (3.17)$$

from Eq. (3.11). Then, the radial potential in Eq. (3.15) can be rewritten as

$$R(r) = -C(r - r_-)(r - r_+), \quad (3.18)$$

with the roots $r_{\pm} = ELC^{-1}(1 \pm \sqrt{1 + CL^{-2}})$. One can compare the values of r_{\pm} with r_c to find the allowed regions of motion. We list the classification below and present the phase space in Fig. 1.

Case 1: $C > 0$ or $C > -L^2$, $L < 0$. In this case, $E > 0$ must be satisfied. There is an outer bound at r_{\pm_L} , where \pm_L is the sign of L . Thus the particles are confined in the region $0 \leq r \leq r_{\pm_L}$ and cannot escape to infinity. In Fig. 1, this case is shown as the light blue region outside the gray curve.

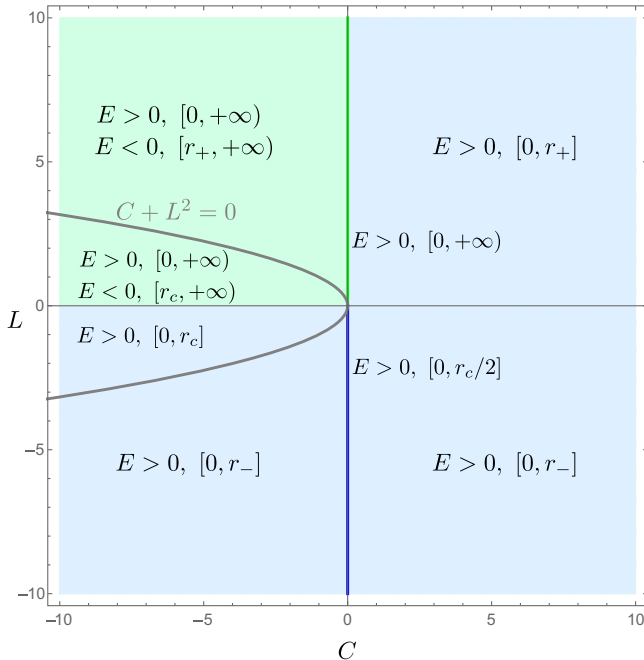


FIG. 1. Phase space of future-directed radial motions.

Case 2: $-L^2 < C < 0$, $L > 0$. If $E > 0$, then the allowed region is $r \in [0, +\infty)$ with no turning point, while $E < 0$, the allowed region becomes $r \in [r_+, +\infty)$, where r_+ is the turning point of the particles. In Fig. 1, we use the light green region outside the gray curve to represent this case.

Case 3: $C < -L^2$. In this case, both $L, E < 0$ are forbidden. If $L, E > 0$, then the allowed region is $r \in [0, +\infty)$. If $L > 0, E < 0$, then the allowed region is $r \in [r_c, +\infty)$. If $L < 0, E > 0$, then the allowed region is $r \in [0, r_c]$. For the latter two cases, the trajectories can reach r_c and change their time directions. In Fig. 1, this case is indicated by the region inside the gray curve. However, this case is excluded by the constraint from θ motion [40] for the geodesics of timelike particles. In the following, we can see that it is also excluded in both the force-free solution Eq. (4.8) and the Wald solution Eq. (4.28).

Case 4: $C = 0$. In this case, $E > 0$ is required. If $L > 0$, then the allowed region is $[0, +\infty)$, which is represented by the green line in Fig. 1. If $L < 0$, then the allowed region is $[0, r_c/2]$, represented by the blue line in Fig. 1.

IV. THE ANGULAR MOTIONS

In this section, we investigate the angular motions of charged particles in the NHEK geometry, in the presence of different MSEM fields. We consider two kinds of MSEM fields, one being the force-free one, the other being the vacuum solution. We pay our attention to not only the equatorial but also off-equatorial motions.

A. General properties

We start with the general properties of the angular potential Eq. (3.16). For an MSEM field, the electromagnetic invariant is

$$-F^2 = -F_{\mu\nu}F^{\mu\nu} = \frac{1}{2\Gamma^2} \left[f(\theta) + \frac{\partial_\theta f(\theta)}{\Lambda} \right] \left[f(\theta) - \frac{\partial_\theta f(\theta)}{\Lambda} \right]. \quad (4.1)$$

The field strength is electric dominant when $-F^2 > 0$, and is magnetic dominant when $-F^2 < 0$. To avoid the singularities at the poles, $\partial_\theta f(0)$ and $\partial_\theta f(\pi)$ should be zero. Near the north pole, the angular potential can be expanded as

$$\Theta(\theta) \approx C + L^2 - 2 - \left[\frac{kf(0) - L}{\theta} \right]^2 + \mathcal{O}(\theta). \quad (4.2)$$

Note that for the angular potential near the south pole, we only need to replace $f(0)$ by $f(\pi)$, so we only give a discussion for the north pole. If $L \neq kf(0)$, then the potential diverges at the pole such that particles can never reach the pole. If $L = kf(0)$, then we have $\Theta(0) = C + k^2 f^2(0) - 2$ and $\Theta'(0) = 0$. Thus, for $C \geq 2 - k^2 f^2(0)$, the

particles can reach the north pole, and when the equality holds, the particles can move along the axis.

Second, the equatorial motions take place only when

$$\Theta(\pi/2) = C + L^2 - 1 - \frac{1}{4}[kf(\pi/2) - L]^2 = 0, \quad (4.3)$$

$$\partial_\theta \Theta(\pi/2) = -\frac{k}{2} \partial_\theta f(\pi/2) [kf(\pi/2) - L] = 0. \quad (4.4)$$

When $\partial_\theta f(\pi/2) = 0$, Eq. (4.4) is always true so that the equatorial motions requires the condition Eq. (4.3), which gives a curve in the parameter space of (C, L) . But when $\partial_\theta f(\pi/2) \neq 0$, there must be $L = kf(\pi/2)$ for the equatorial motions. As a result, in the parameter space the equatorial motions correspond to a point $(1 - L^2, L = kf(\pi/2))$ combined with the solution curve of Eq. (4.3). Moreover, the stability of equatorial motion is determined by

$$\begin{aligned} \partial_\theta^2 \Theta(\pi/2) &= -2 - \frac{1}{2} [k \partial_\theta f(\pi/2)]^2 - \frac{1}{2} [L - kf(\pi/2)] \\ &\quad \times [3L - 3kf(\pi/2) - k \partial_\theta^2 f(\pi/2)]. \end{aligned} \quad (4.5)$$

The unstable/stable motions correspond to $\partial_\theta^2 \Theta(\pi/2) \geq 0$. If $\partial_\theta f(\pi/2) = 0$, then $\Theta''(\pi/2)$ becomes a function of L , so that the stability depends on the value of L . In the case $\partial_\theta f(\pi/2) \neq 0$, $L = kf(\pi/2)$, the equatorial trajectories are always stable since the term $-2 - \frac{1}{2} [k \partial_\theta f(\pi/2)]^2$ in the Eq. (4.5) is always negative.

B. Force-free solution

In this subsection, we focus on the force-free solution² in which the source feels a vanishing Lorentz force,

$$J^\mu F_{\mu\nu} = 0. \quad (4.6)$$

On the other hand, from the Maxwell equation $\nabla_\mu F^{\mu\nu} = J^\nu$, we can get

$$J^\mu \partial_\mu = -\frac{1}{2\Gamma^2 \Lambda} \left[\partial_\theta \left(\frac{\partial_\theta f(\theta)}{\Lambda} \right) + \Lambda f(\theta) \right] \partial_\phi, \quad (4.7)$$

which is a pure toroidal current since only the ϕ component of J^μ survives. Combining with Eq. (4.6), we find that $f(\theta) = f_0$ must be a constant and

$$A = f_0(d\phi + rdt), \quad J^\mu \partial_\mu = -\frac{2f_0}{1 + \cos^2 \theta} \partial_\phi, \quad (4.8)$$

²The force-free fields have been explored to approximate black hole magnetospheres [48]. In the NHEK geometry, the force-free condition is equal to the degenerate condition, $(\star F)_{\mu\nu} F^{\mu\nu} = 0$.

which describes an electric-dominated field outside the ergosphere.³ Considering the fact that the system of interest has the Z_2 symmetry ($\theta \rightarrow \pi - \theta$), so we only focus on $0 \leq \theta \leq \pi/2$ without losing generality. It is convenient to define

$$z = \cos^2 \theta, \quad (4.9)$$

then Eqs. (3.14) and (3.16) can be rewritten as

$$\Gamma \frac{dz}{d\tau} = \pm_\theta \sqrt{z \Theta_{\text{FF}}(z)} = \pm_\theta \sqrt{z(\mathbf{a}z^2 + \mathbf{b}z + \mathbf{c})}, \quad (4.10)$$

$$\begin{aligned} \mathbf{a} &= 1 - \frac{1}{4}(L - \mathcal{E})^2, & \mathbf{b} &= -C - \frac{3}{2}L^2 + \mathcal{E}L - \frac{1}{2}\mathcal{E}^2, \\ \mathbf{c} &= C + L^2 - 1 - \frac{1}{4}(L - \mathcal{E})^2, \end{aligned} \quad (4.11)$$

with $\mathcal{E} = kf_0$ being the electromagnetic parameter. The angular potential $\Theta_{\text{FF}}(z)$ has two roots $z_\pm = \frac{1}{2\mathbf{a}}(-\mathbf{b} \pm \sqrt{\mathbf{b}^2 - 4\mathbf{a}\mathbf{c}})$. Note that at the north pole, $z = 1$, and the angular potential $\Theta_{\text{FF}}(z)$ becomes

$$\Theta_{\text{FF}}(1) = \mathbf{a} + \mathbf{b} + \mathbf{c} = -(L - \mathcal{E})^2, \quad (4.12)$$

which is negative when $L \neq \mathcal{E}$. Considered $\Theta_{\text{FF}}(0) = \mathbf{c}$, the allowed region of motion is $z \in [0, z_{\mp\mathbf{a}}]$ with $\mp_{\mathbf{a}}$ being minus the sign of \mathbf{a} , when $\mathbf{c} > 0$. In this case, the particles oscillate between $\theta_- = \cos^{-1} \sqrt{z_{\mp\mathbf{a}}}$ and $\theta_+ = \pi - \cos^{-1} \sqrt{z_{\mp\mathbf{a}}}$, crossing the equatorial plane for each oscillation. These trajectories are usually called ‘‘oscillatory’’ motions. The yellow and orange regions in the phase spaces in Fig. 2 represent the oscillatory motions for $\mathbf{a} < 0$ and $\mathbf{a} > 0$, respectively. Actually, in the force-free field, there holds

$$\begin{aligned} \mathbf{c} &= C + L^2 - 1 - \frac{1}{4}(L - \mathcal{E})^2 \geq C + L^2 - 2\Gamma - \frac{1}{\Lambda^2}(L - \mathcal{E})^2 \\ &= \Theta_{\text{FF}}(z) \geq 0. \end{aligned} \quad (4.13)$$

In Fig. 2 the case $\mathbf{c} < 0$ is indicated by the red color, labeled as the forbidden regions. When $\mathbf{c} = 0$, the particles can move in the equatorial plane with

$$C_{\text{eq}} = 1 - \frac{3}{4}L_{\text{eq}}^2 - \frac{1}{2}\mathcal{E}L_{\text{eq}} + \frac{1}{4}\mathcal{E}^2, \quad (4.14)$$

and the stability is determined by $\partial_z \Theta_{\text{FF}}(0) = -1 - 3(L_{\text{eq}} - \mathcal{E})^2/4 < 0$. Thus, all the equatorial motions are stable, represented by the orange curves in Fig. 2.

Except for the special case $\mathbf{c} = 0$, we can conclude that only the oscillatory motions are allowed. This picture can

³There is no global timelike Killing vector in NHEK, and only the region outside the ergosphere are the physical region of electromagnetic fields [61].

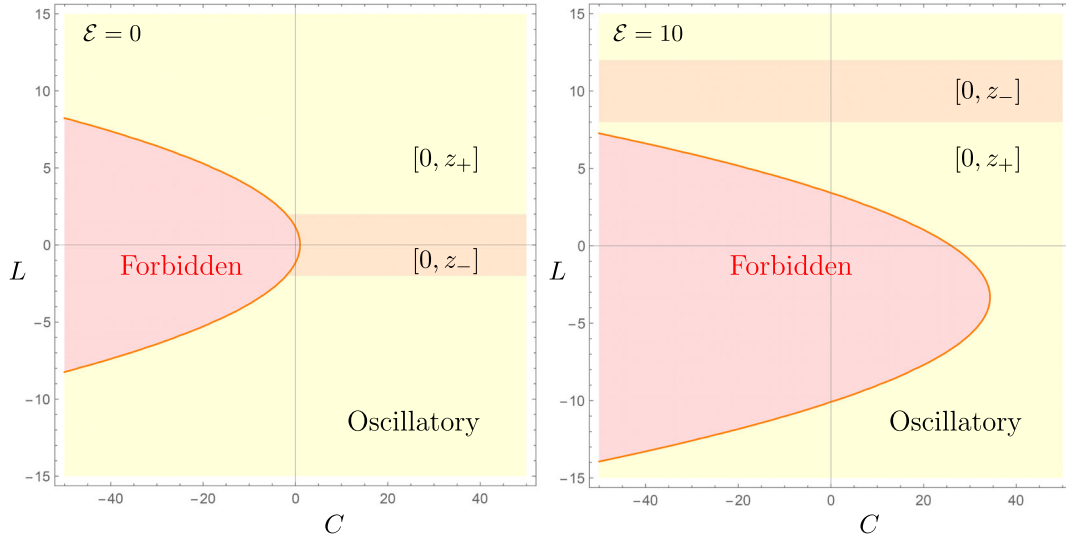


FIG. 2. Phase spaces of angular motions in the force-free field.

be inferred from the study of the geodesics in the NHEK geometry. It has been shown in [40] that the NHEK geodesics are all oscillatory and the angular potential of the NHEK geodesics takes the form of Eq. (3.16) with $f(\theta) = 0$. In our force-free case, we have $f(\theta) = f_0$ as a constant so that the angular potential is simply modified by adding a constant.

Moreover, it can be checked that $C + L^2 > \mathbf{c} \geq 0$ for all the equatorial and off-equatorial motions. This ensures that a charged particle can never reach r_c and that the time direction is kept unchanged in the force-free field considering the radial potential discussed in Sec. III B.

C. Vacuum solution

Next we turn to another class of MSEM fields, which are produced by the sources outside the NHEK region. In this case, we have $J^\mu = 0$ in the Eq. (4.7) and obtain the vacuum solution

$$\mathcal{A} = \left(A_M \frac{\sin^2 \theta}{1 + \cos^2 \theta} + A_E \frac{2 \cos \theta}{1 + \cos^2 \theta} \right) (d\phi + r dt). \quad (4.15)$$

The parameters A_M, A_E are real constants, which can be taken as magnetic and electric fields in the sense that near the axis, the electromagnetic invariant becomes

$$-F^2 \approx (A_E^2 - A_M^2)/2. \quad (4.16)$$

We define

$$u = \cos \theta, \quad (4.17)$$

and the angular equation can be rewritten as

$$2\Gamma \frac{du}{d\tau} = \mp_\theta \sqrt{\Theta_v(u)}, \quad (4.18)$$

with the angular potential

$$\begin{aligned} \Theta_v(u) = & \left(1 - \frac{L^2}{4} \right) u^4 - \left(C + \frac{3}{2} L^2 \right) u^2 + C + \frac{3}{4} L^2 - 1 \\ & - \left(\frac{kA_M L}{2} + \frac{k^2 A_M^2}{4} \right) u^4 - (kA_E L + k^2 A_M A_E) u^3 \\ & + k^2 \left(\frac{A_M^2}{2} - A_E^2 \right) u^2 + (kA_E L - k^2 A_M A_E) u \\ & + k \frac{A_M L}{2} - k^2 \frac{A_M^2}{4}. \end{aligned} \quad (4.19)$$

One can see that this potential is invariant under $L \rightarrow -L$, $A_M \rightarrow -A_M$, $A_E \rightarrow -A_E$. Note that the system does not have Z_2 symmetry ($\theta \rightarrow \pi - \theta$), which complicates the classification of motions.

We consider two special cases here before we discuss the more general cases. The first special case is that of the equatorial motions, which requires

$$\Theta_v(0) = \partial_u \Theta_v(0) = 0, \quad (4.20)$$

and then

$$\begin{aligned} L_{\text{eq}} = & \begin{cases} \text{arbitrary value,} & \text{if } A_E = 0 \\ kA_M, & \text{if } A_E \neq 0 \end{cases}, \\ C_{\text{eq}} = & 1 + \frac{1}{4} (k^2 A_M^2 - 2kA_M L_{\text{eq}} - 3L_{\text{eq}}^2). \end{aligned} \quad (4.21)$$

As discussed in Sec. IV A, if $A_E = 0$, then there exists a class of equatorial motions with various L , but if $A_E \neq 0$,

then the equatorial trajectories must have fixed parameters. The stability is determined by the sign of

$$\partial_u^2 \Theta_v(u)|_{\text{eq}} = -1 - k^2 A_E^2 + \frac{1}{4}(kA_M + 3L_{\text{eq}})(kA_M - L_{\text{eq}}), \quad (4.22)$$

where the subscript ‘‘eq’’ means that the function takes value at $L = L_{\text{eq}}$, $C = C_{\text{eq}}$, and $u = 0$. For a nonvanishing A_E , $\partial_u^2 \Theta_v(u)|_{\text{eq}} = -1 - k^2 A_E^2 < 0$, which means that the equatorial trajectories are always stable. The case $A_E = 0$

with generic trajectories will be discussed carefully in the next subsection.

The second special case is a type of motion that lies on conical surfaces which are determined by

$$\Theta_v(u) = 0, \quad \partial_u \Theta_v(u) = 0, \quad u \neq 0. \quad (4.23)$$

Such kind of conical motion is absent in the NHEK geodesics. In this kind of motion, the conserved quantities in the parameter space are constrained by the above relation (4.23),

$$\begin{aligned} L_{\pm}(u) &= \frac{kA_M(1-u^2)^2 u + kA_E(u^4 - 4u^2 - 1) \pm (1-u^2)X}{u(3-u^2)(1+u^2)}, \\ C_{\pm}(u) &= \frac{Y \mp [2kA_M(3-2u^2+3u^4)u - kA_E(3+15u^2-3u^4+u^6)](1-u^2)X}{2(3-u^2)^2(1+u^2)^2 u^2}, \end{aligned} \quad (4.24)$$

where

$$\begin{aligned} X &= \sqrt{k^2 A_M^2 (u^2 + 4)u^2 + k^2 A_E^2 (1 - u^2)^2 + 4k^2 A_M A_E (1 - u^2)u - 4(3 - u^2)(1 + u^2)u^2}, \\ Y &= -2k^2 A_M^2 (3 - 14u^2 + 12u^4 - 2u^6 + u^8)u^2 - k^2 A_E^2 (3 + 9u^2 + 42u^4 - 26u^6 + 3u^8 + u^{10}) \\ &\quad + 32k^2 A_M A_E (1 - u^2)^2 u^3 + 4(9 + 2u^4 + 8u^6 - 3u^8)u^2. \end{aligned} \quad (4.25)$$

Note that X^2 must be non-negative, which gives a constraint on the allowed region of u . As these expressions are very complicated, we would not like to give a detailed discussion on this case. Instead, we will focus on a simple case $A_E = 0$ in the following, since $A_E = 0$ implies that the gauge potential is magnetic dominant, which is a more realistic situation in astrophysics.

1. Angular potential and off-equatorial motions

In the following, we take $A_E = 0$ in the vacuum solution. When $A_E = 0$, the vacuum solution Eq. (4.15) actually reduces to the Wald potential in the near-horizon limit [60]. To clarify this point, recall that the Wald vector potential in the Boyer-Lindquist coordinates takes the form

$$\mathcal{A}_W = (aB - Q/2)\partial_{\tilde{t}} + (B/2)\partial_{\tilde{\phi}}, \quad (4.26)$$

where Q is the charge of the black hole, and B is a test magnetic field vertical at infinity. When zooming into the NHEK region by Eq. (2.4), we have

$$2\partial_{\tilde{t}} = \epsilon^p \partial_t - \partial_{\phi}, \quad \partial_{\tilde{\phi}} = \partial_{\phi}. \quad (4.27)$$

In the leading order, only the field produced by the charge survives, and the vector potential reduces to [47]

$$\mathcal{A}_W = \frac{Q}{4} \partial_{\phi}, \quad (4.28)$$

which is the same as the field (4.15) if we identify $Q = A_M$. The physical reason why we drop the test magnetic field in the Wald vector potential is that the extreme black hole behaves like a perfect diamagnet, excluding the lines of test magnetic fields [62], and only the intrinsic field provided by Q survives. Moreover, although the test magnetic term in the potential is dropped, the charge Q still generates a magnetic dipole due to the fast rotation of the black hole, so that the Eq. (4.28) describes a magnetic-dominated case, i.e., $-F^2 < 0$ outside the ergosphere.

Now we turn to study the angular potential in the background of Eq. (4.28). We will concern the off-equatorial motions especially. Note that the system has an Z_2 symmetry ($\theta \rightarrow \pi - \theta$), so we consider $0 \leq \theta \leq \pi/2$ without loss of generality. By defining

$$z = \cos^2 \theta, \quad (4.29)$$

we can obtain a quadratic angular potential and find

$$\Gamma \frac{dz}{d\tau} = \pm_{\theta} \sqrt{z \Theta_W(z)} = \pm_{\theta} \sqrt{z(\mathbf{a}z^2 + \mathbf{b}z + \mathbf{c})}, \quad (4.30)$$

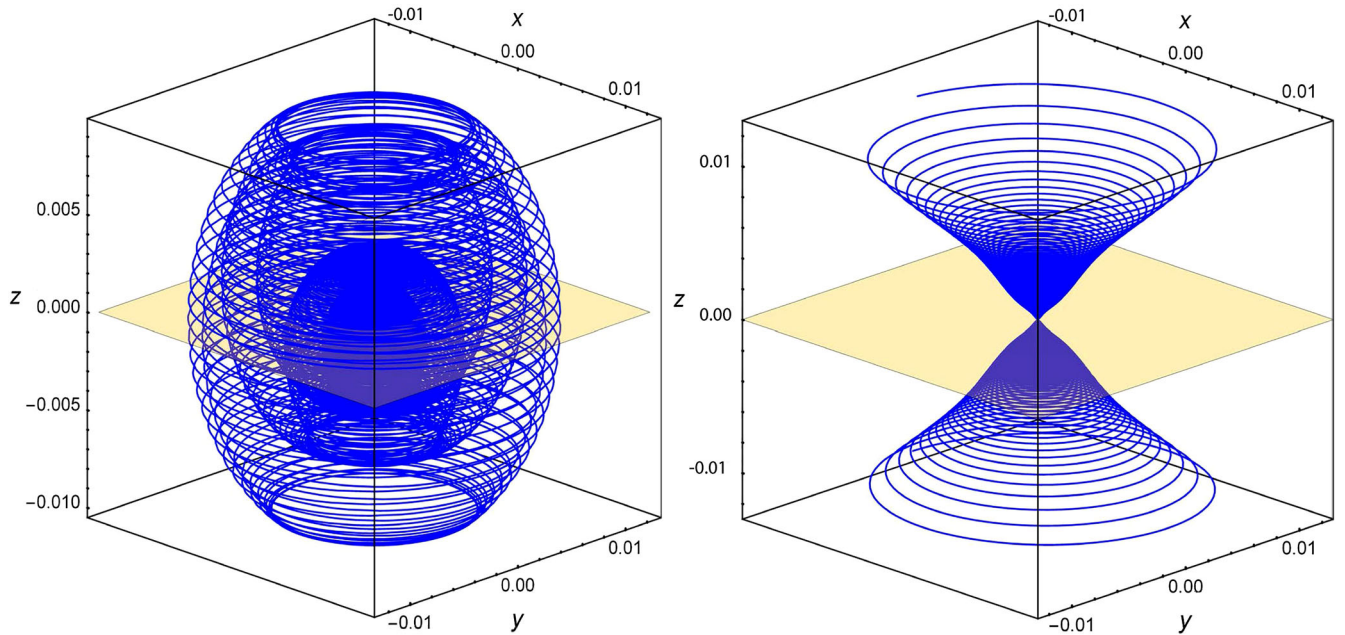


FIG. 3. Left: the trajectory of an oscillatory motion with the initial parameter chosen as $\mathfrak{B} = 50$, $(E, L, C) = (20, 30, 100)$, $r = 0.01$, and $\theta = \pi/2$. Right: the trajectories of two symmetric vortical motions with the initial parameter chosen as $\mathfrak{B} = 50$, $(E, L, C) = (5, 15, -220)$, $r = 0.01$, and $\theta = \pi/4$ (above), $3\pi/4$ (below). For a better display, the trajectories are plotted in the coordinate: $x = \epsilon_0 r \sin \theta \cos(\phi + t/\epsilon_0)$, $y = \epsilon_0 r \sin \theta \sin(\phi + t/\epsilon_0)$, $z = \epsilon_0 r \cos \theta$, with $\epsilon_0 = 0.001$. The event horizon is at $(0,0,0)$, and the yellow planes denote the equatorial plane.

$$\begin{aligned} a &= 1 - \frac{1}{4}(L + \mathfrak{B})^2, & b &= -C - \frac{3}{2}L^2 + \frac{1}{2}\mathfrak{B}^2, \\ c &= C + \frac{1}{4}(L + \mathfrak{B})(3L - \mathfrak{B}) - 1, \end{aligned} \quad (4.31)$$

where we have introduced an electromagnetic parameter $\mathfrak{B} = kQ$. In addition, considering that the potential is invariant under $L \rightarrow -L$, $\mathfrak{B} \rightarrow -\mathfrak{B}$, we may set $\mathfrak{B} \geq 0$ for simplicity. It should be stressed that the Eq. (4.30) has appeared in [47], where the authors investigated the special cases that charged particles move along the axis and on the equatorial plane. However, in the present work we mainly focus our attention to general off-equatorial motions and quantitatively study the effect of the electromagnetic field. Hence, we need a detailed analysis of the angular potential in the Eq. (4.30).

Obviously, the equation

$$\Theta_{\text{W}}(z) = az^2 + bz + c = 0 \quad (4.32)$$

has two roots at $z_{\pm} = (-b \pm \sqrt{b^2 - 4ac})/2a$. And at the poles the potential becomes

$$\Theta_{\text{W}}(1) = a + b + c = -L^2. \quad (4.33)$$

The special case $L = 0$ indicates that the trajectories might cross the pole. It is beyond our interest, so we focus on $L \neq 0$ in the following. Therefore, we have $\Theta_{\text{W}}(1) < 0$. On

the other hand, we find $\Theta_{\text{W}}(0) = c$. It is worth mentioning that for the force-free case, the angular potential is always non-negative at $z = 0$, considering Eq. (4.13). However, due to a nontrivial influence of \mathfrak{B} on the angular potential in the vacuum solution, the sign of c is uncertain, and the motions of charged particles need a detailed discussion.

We first consider the case $c > 0$. In this case $\Theta_{\text{W}}(0) > 0$ so that the charged particles move along normal oscillatory trajectories, and the allowed region is $z \in [0, z_{\mp a}]$, with $\mp a$ being minus the sign of a . As an example, an oscillatory trajectory is shown in the left plot in Fig. 3. We also present the oscillatory motions for $a < 0$ and $a > 0$ in the phase space indicated by the yellow and orange regions in the top left figure of the Fig. 4, respectively, where we set $\mathfrak{B} = 10$.

Then we move to the case $c < 0$. The motions of charged particles must satisfy $z \in [0, 1]$, such that the coefficients have to obey

$$a < 0, \quad 0 < -\frac{b}{2a} < 1, \quad b^2 - 4ac \geq 0. \quad (4.34)$$

If the above inequalities can be satisfied, then the polar angles of charged particles oscillate between $\theta_- = \cos^{-1} \sqrt{z_+}$ and $\theta_+ = \cos^{-1} \sqrt{z_-}$, or $\pi - \theta_+$ and $\pi - \theta_-$, without crossing the equatorial plane, and such trajectories are the so-called vortical motions. Likewise, we present an example of a pair of vortical motions in the right plot of Fig. 3, which are symmetric about the equatorial plane and reflects the symmetric transformation $\theta \rightarrow \pi - \theta$,

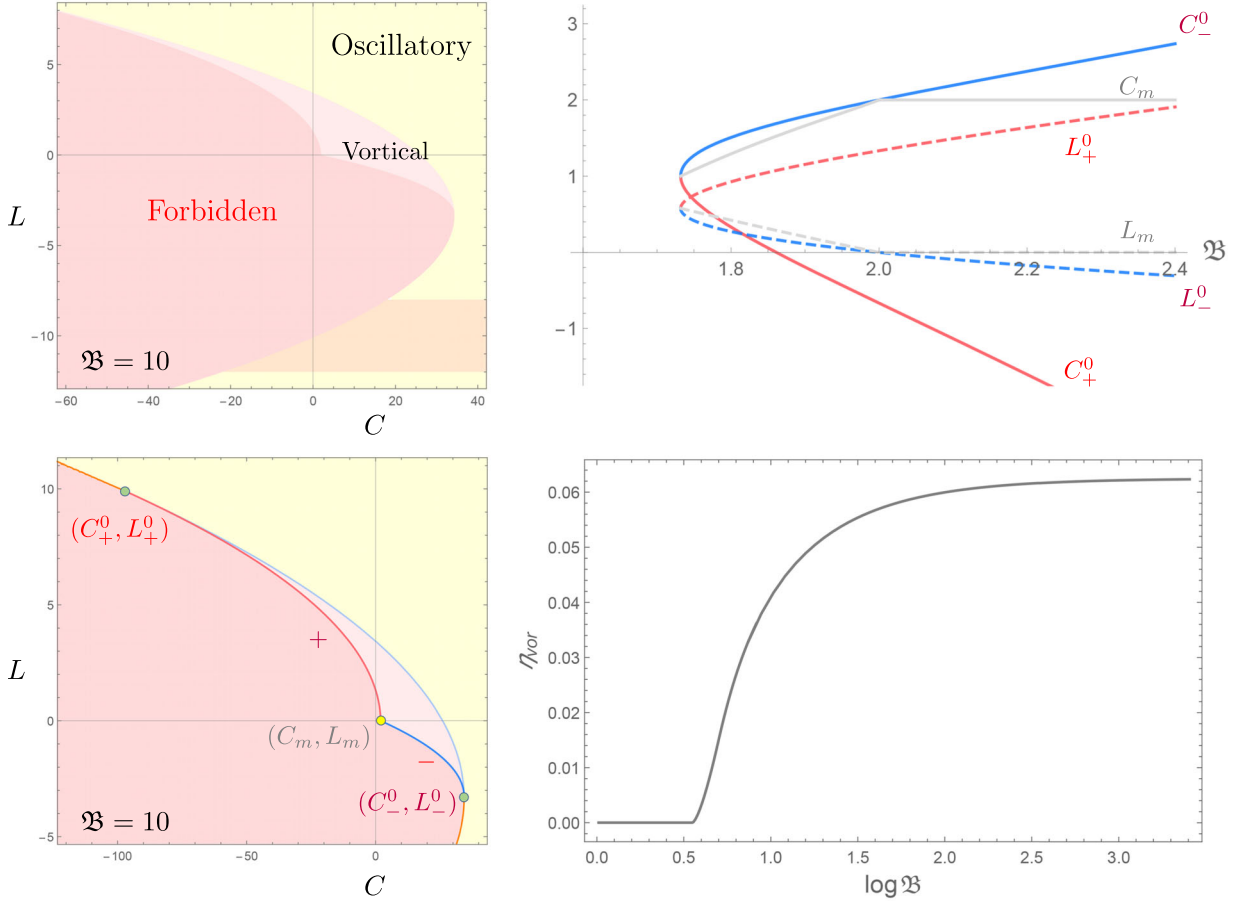


FIG. 4. Top left: phase space of angular motions in the Wald potential with $\mathfrak{B} = 10$. The phase spaces with larger \mathfrak{B} are qualitatively similar. Down left: end points of two branches of conical motions with $\mathfrak{B} = 10$. Top right: the end points and the cusp are plotted as the functions of \mathfrak{B} . The plot region is $\mathfrak{B} \in [1.6, 2.4]$. Bottom right: η_{vor} as a function of $\log \mathfrak{B}$. The plot region is $\mathfrak{B} \in [1, 30]$.

$\phi \rightarrow \phi + \pi$, $\pm_\theta \rightarrow \mp_\theta$ in Eq. (4.30). In addition, in the top left figure in Fig. 4, we also show the vortical motions in the phase space which are indicated by the gray color. Considering the fact that there are no vortical motions for the geodesics in the NHEK region [40], we can easily conclude that these vortical motions are caused by the electromagnetic force.

At last, we give a brief discussion on the case $\mathbf{c} = 0$. In this case, we have $\Theta_{\text{W}}(z=0) = \mathbf{c} = 0$, which corresponds to

$$\Theta_{\text{W}}\left(\theta = \frac{\pi}{2}\right) = \partial_\theta \Theta_{\text{W}}\left(\theta = \frac{\pi}{2}\right) = 0, \quad (4.35)$$

and

$$\begin{aligned} \partial_\theta^2 \Theta_{\text{W}}\left(\theta = \frac{\pi}{2}\right) &\propto \partial_z \Theta_{\text{W}}(z=0) \\ &= -1 + (\mathfrak{B} + 3L)(\mathfrak{B} - L)/4. \end{aligned} \quad (4.36)$$

When $\partial_z \Theta_{\text{W}}(z=0) \leq 0$, the potential $\Theta_{\text{W}}(z)$ is a decreasing function in $z \in [0, 1]$, thus the particles are confined to the

equatorial plane and the trajectories are stable. When $\partial_z \Theta_{\text{W}}(z=0) > 0$, $\Theta_{\text{W}}(z)$ increases to a peak and then decreases in $z \in [0, 1]$, and $z=0$ is an unstable extremal point of $\Theta_{\text{W}}(z)$, corresponding to unstable equatorial motion.

In addition, we want to emphasize that all the motions discussed above satisfy $C + L^2 \geq 0$ (see proof in the Appendix), which means a charged particle never reaches r_c and is always future directed in the Wald potential.

2. More on vortical motions and astrophysical implications

In this subsection, we would like to illustrate the features of the phase space more carefully. In particular, we want to give a more detailed analysis of the vortical motions.

First, it is worth mentioning that there are vortical motions only in the vacuum solution, and no such motions in the force-free model. It is expected that the force-free model would be a good approximation of the magnetosphere away from the equatorial plane based on simulations. However, it should be noted that the force-free MSEM considered in this work assumes maximal symmetry, which is an oversimplification and idealization

compared to normal force-free solutions in astrophysical research. It would be interesting to see if vortical motion can appear with the assumption being relaxed.

Then, let us focus on the boundaries of the vortical motions in the phase space. It is convenient to zoom in on the gray region of the top left plot in Fig. 4 to get the bottom left plot. In the bottom left plot of Fig. 4, one can see that the orange and light blue curves represent the stable and unstable equatorial motions at $\mathbf{c} = 0$. In other words, the stable equatorial motions form the boundary of the oscillatory motions, and the unstable equatorial motions form the dividing line between the oscillatory and vortical motions in the phase space. Apparently, there could be other critical motions that form the boundaries of the vortical motions in the phase space.

For these additional critical motions, we have $z_- = z_+$ corresponding to a constant θ , which is a simplified case of Eq. (4.23). In this case, the charged particles are moving on conical surfaces and the trajectories are determined by

$$\Theta_W(z) = \Theta'_W(z) = 0. \quad (4.37)$$

For simplicity, we would like to call them the conical motions which are short for the motions on the conical surfaces. The corresponding conserved quantities take the form

$$\begin{aligned} L_{\pm}(z) &= \frac{\mathfrak{B}(z-1)^2 \pm 2(1-z)X}{(z+1)(3-z)}, \\ C_{\pm}(z) &= \frac{Y \mp 2\mathfrak{B}(3z^2 - 2z + 3)(1-z)X}{(z+1)^2(3-z)^2}, \end{aligned} \quad (4.38)$$

where we introduced

$$\begin{aligned} X &= \sqrt{z^2 - 2z + \mathfrak{B}^2 - 3}, \\ Y &= -(\mathfrak{B}^2 + 6)z^4 + 2(\mathfrak{B}^2 + 8)z^3 + 4(1 - 3\mathfrak{B}^2)z^2 \\ &\quad + 14\mathfrak{B}^2z + 18 - 3\mathfrak{B}^2. \end{aligned} \quad (4.39)$$

The condition $X^2 \geq 0$ leads to

$$z^2 - 2z + \mathfrak{B}^2 - 3 \geq 0, \quad (4.40)$$

which requires that $\mathfrak{B}^2 - 3$ be non-negative in order that the above inequality can be obeyed for $z \in [0, 1]$. As a result, we obtain a critical value of the electromagnetic parameter as

$$\mathfrak{B}_c = \sqrt{3}. \quad (4.41)$$

When $\mathfrak{B} < \mathfrak{B}_c$, there is no conical motion, and consequently the vortical motions do not exist as well. Simply speaking, $\mathfrak{B} \geq \mathfrak{B}_c$ is a necessary condition to have vortical motions.

When the condition $\mathfrak{B} \geq \mathfrak{B}_c$ holds, there are two branches $L_+(C_+)$ and $L_-(C_-)$ from Eq. (4.38), corresponding to two smooth curves in the phase space. In the bottom left plot of Fig. 4, we set $\mathfrak{B} = 10 > \sqrt{3}$ so that the vortical and conical motions exist; $L_+(C_+)$ and $L_-(C_-)$ are marked by the red and dark blue curves, respectively, and their intersection is given by (C_m, L_m) . Moreover, we use (C_+^0, L_+^0) to denote the intersection of the light blue and the red curves, and (C_-^0, L_-^0) to represent the intersection of the light blue and the dark blue curves, where the light blue one is a portion of the curve determined by $\mathbf{c} = 0$. Now, we see that when $\mathfrak{B} > \mathfrak{B}_c$ the existing vortical motions are bounded by the curves $L_+(C_+)$, $L_-(C_-)$, and $\mathbf{c} = 0$ with a few intersection points.

The values of the intersection points (C_+^0, L_+^0) , (C_-^0, L_-^0) , and (C_m, L_m) can be determined for a fixed \mathfrak{B} . Combining $\mathbf{c} = 0$ and $L = L_+(C_+)$, we obtain that at $z = 0$

$$\begin{aligned} L_{\pm}(0) &= L_{\pm}^0 = \frac{1}{3}\mathfrak{B} \pm \frac{2}{3}\sqrt{\mathfrak{B}^2 - \mathfrak{B}_c^2}, \\ C_{\pm}(0) &= C_{\pm}^0 = 2 - \mathfrak{B}L_{\pm}^0, \end{aligned} \quad (4.42)$$

which means the solid angle of the conical plane is 2π and the conical plane coincides with the equatorial plane. On the other hand, the non-negativity of X^2 gives an upper limit of z , $z = z_m$. For the case $\mathfrak{B}_c < \mathfrak{B} < 2$, we have $z_m = 1 - \sqrt{4 - \mathfrak{B}^2}$ and

$$\begin{aligned} L_{\pm}(z_m) &= L_m = \frac{4}{\mathfrak{B}} - \mathfrak{B}, \\ C_{\pm}(z_m) &= C_m = \sqrt{4 - \mathfrak{B}^2} \left(\frac{8}{\mathfrak{B}^2} - 2 \right) - \mathfrak{B}^2 - \frac{32}{\mathfrak{B}^2} + 14. \end{aligned} \quad (4.43)$$

For the case $\mathfrak{B} > 2$, we always have $z_m = 1$, and $(C_m, L_m) \equiv (2, 0)$, which corresponds to the motions along the spin axis. The behaviors of $C_{\pm}^0, L_{\pm}^0, C_m, L_m$ as the functions of \mathfrak{B} are shown in the top right plot of Fig. 4. For $\mathfrak{B} = \mathfrak{B}_c$, all the points coincide with $L = 1/\sqrt{3}$, $C = 1$. Moreover, in the case that $\mathfrak{B}_c < \mathfrak{B} < 2$ all the conical motions are prograde as $\Lambda_{\pm}^0 > 0$, while in the case that $\mathfrak{B} > 2$, the conical motion could be prograde with $L_+^0 > 0$ as well as retrograde with $L_-^0 < 0$.

Next, we consider the stability of the conical motions. From Eqs. (4.30) and (4.38), we can easily have $\partial_z^2 \Theta_W(z) \leq 0$, which means the conical motions are always stable. Moreover, $L_+^0(C_+^0), L_-^0(C_-^0)$ correspond to marginal stable motions, since in this case $\partial_z^2 \Theta_W(z) = 0$. Since the conical motions form the boundary of the vortical motions, they will change into the vortical motions and swing slightly around the original conical surface under a perturbation of the conserved quantities.

Furthermore, since the vortical motions are bounded, the area of the vortical motions in the phase space should be finite. To characterize the ratio of the vortical motions in the phase space, we would like to introduce a parameter η_{vor} as

$$\eta_{\text{vor}} = \int_{\text{vor}} \frac{dCdL}{S_0}, \quad (4.44)$$

where ‘‘vor’’ means an integration in the vortical region, and S_0 is defined as the area of the rectangle⁴ bounded by the straight lines $C = C_{\pm}$ and $L = L_{\pm}$. From Eq. (4.42) we have

$$S_0 = (C_-^0 - C_+^0)(L_+^0 - L_-^0) = 16\mathfrak{B}(\mathfrak{B}^2 - 3)/9. \quad (4.45)$$

Strictly speaking, η_{vor} is not the ratio of the vortical motions in the whole phase space, it only characterizes the ratio of the vortical motions in the space enclosed by the rectangle. It is straightforward to compute η_{vor} , with the help of the expressions of the conical motions. The bottom right plot of Fig. 4 shows the result of η_{vor} as a function⁵ of \mathfrak{B} . Note that for

$$\mathfrak{B} = \mathfrak{B}_c + \delta\mathfrak{B}, \quad 0 < \delta\mathfrak{B} \ll 1, \quad (4.46)$$

we have

$$S_0 \approx 10.66 \delta\mathfrak{B} \quad \text{and} \quad \int_{\text{vor}} dCdL \approx 0.51(\delta\mathfrak{B})^2. \quad (4.47)$$

Thus, η_{vor} is of $\mathcal{O}(\delta\mathfrak{B})$ near $\mathfrak{B} = \mathfrak{B}_c$. When \mathfrak{B} is increasing, η_{vor} is getting larger, which implies that the enlarged electromagnetic field triggers more vortical motions of charged particles. However, as \mathfrak{B} increases enough, we have $\eta_{\text{vor}} \rightarrow 0.062$. In this case, the system is almost completely dominated by the Lorentz force, and the phase space gains an emergent symmetry, that is, $\mathfrak{B} \rightarrow \lambda\mathfrak{B}$, $L \rightarrow L/\lambda$, $C \rightarrow C/\lambda^2$, where λ is the scaling factor.

The novel features related to a charged black hole discussed above might have some astrophysical significance. In the Gauss unit, for a particle of charge q and mass m , there is

$$\mathfrak{B} = \frac{1}{G} \frac{q}{m} \frac{Q}{M} \sim 3 \times 10^{22} \left(\frac{q}{e}\right) \left(\frac{m_p}{m}\right) \left(\frac{Q}{\sqrt{GM}}\right), \quad (4.48)$$

⁴By Eq. (4.38) one finds that both $L_+(C_+)$ and $L_-(C_-)$ are decreasing functions of C_+ and C_- , respectively. Then in the phase space, the parabolic curve determined by $\mathfrak{c} = 0$ has an extreme point with $L = -\mathfrak{B}/3 < L_-^0$. Thus, the rectangle encloses the vortical region in the phase space.

⁵When we extend to the regime $\mathfrak{B} < \mathfrak{B}_c$, the expression of S_0 still holds, but there is no vortical motion. Nevertheless, we may define $\eta_{\text{vor}} \equiv 0$ for $\mathfrak{B} \leq \mathfrak{B}_c$ and obtain the straight interval for $0 \leq \mathfrak{B} < \mathfrak{B}_c$ in the bottom right plot of Fig. 4.

where e is the unit charge, m_p is the ion’s mass (the hydrogen nucleus), and Q is the black hole charge. Astronomically, the black hole accretes hot plasma to the near-horizon region, forming a disk region near the equatorial plane. Moreover, abundant collisionless particles can be accreted or produced outside the disk region [63], where they are accelerated by the magnetosphere and emit nonthermal synchrotron radiation. Note that the single-particle approximation only applies outside the disk region, thus only the vortical motions can produce nonthermal radiations in NHEK geometry. Considering the radiations could escape to infinity, the signature of the charged particles moving vortically might be observed by the telescopes.

On the other hand, as the specific charge of electron is much larger than that of ions, so that $\mathfrak{B}_e \approx 2000\mathfrak{B}_{\text{ion}}$. If $\mathfrak{B}_e \lesssim \mathfrak{B}_c$, then there are only oscillatory motions and no nonthermal radiations. If $\mathfrak{B}_i \lesssim \mathfrak{B}_c < \mathfrak{B}_e$, then only electrons can move vortically, while if $\mathfrak{B}_i > \mathfrak{B}_c$, then both electrons and ions can move vortically. As an example, for a supermassive black hole with mass $M = 10^{10}M_{\odot}$, as long as the black hole charge Q is larger than $1.4C$, the radiations from near-horizon vortical electrons could be observed. However, the radiations from near-horizon vortical ions could be observable only when $Q > 2800C$.

Finally, we would like to comment on the extraction of rotational energy through electromagnetic fields. The Blandford-Znajek mechanism [64] states that the energy of a Kerr black hole can be extracted through magnetic field torsion in the form of Poynting flux based on the force-free solution. On the contrary, unlike the force-free solution, the vacuum solution cannot generate an energy flux from the horizon, suggesting that energy extraction through the vacuum electromagnetic field is not feasible. Additionally, as the NHEK spacetime on which the present work based is not asymptotically flat, a more careful analysis is required to see if the vortical motion can be extended to the asymptotical flat region and check the efficiency of energy extraction.

V. SUMMARY AND DISCUSSION

In this work, we studied the motions of charged particles under MSEM fields in the NHEK geometry. Due to the enhanced symmetry, there are enough conserved quantities to simplify the equations of motion, which turn out to be only a set of decoupled first-order differential equations. Even though the radial motions are similar to the geodesics in NHEK, the angular motions are changed significantly by the electromagnetic fields. We investigated the motions of charged particles in two MSEM fields, the force-free field and the field in vacuum solutions. In the force-free case, there are stable equatorial motions and oscillatory motions, similar to the geodesics in NHEK. In the vacuum solution, we mainly focused on the case that $A_E = 0$, which recovers

the Wald potential in the NHEK geometry, and discussed the motions of charged particles in detail.

The motions of charged particles under the Wald potential in NHEK geometry present some novel features. In the NHEK region, the Wald potential is dominated by an electromagnetic field Eq. (4.28). In this case, the angular motions could be classified into two types, one being the oscillatory motions that cross the equatorial planes continually, and the other being the vortical motions without crossing the equatorial plane. We found the critical value of the electromagnetic parameter $\mathfrak{B}_c = \sqrt{3}$ above which the vortical motions would occur. Among the vortical motions, there is a special subclass of motions, in which the particles move in a conical surface with fixed θ . Actually in the “phase space” of the motions Fig. 4, the vortical motions are surrounded by the conical motions and unstable equatorial motions. We calculated the conserved quantities of the conical motions and showed their changes with \mathfrak{B} in the top right plot of the Fig. 4.

In addition, since the electromagnetic field can be seen as a magnetosphere produced by a weakly charged black hole, we further discussed some astrophysical implications of \mathfrak{B}_c and found that even a weak black hole charge might induce a significant difference between the behaviors of electrons and ions in NHEK geometry, thus triggering relevant observational signatures.

We close this paper with some outlooks. On the one hand, as the first step to considering more realistic models, the discussion is limited to charged particle dynamics in the NHEK geometry with a weak electromagnetic field. It would be interesting to consider the effect of a strong field that affects the background geometry, like the near-horizon description of extreme Ernst-Wild solution and extreme MKN black holes [65]. On the other hand, it is of both theoretical and astrophysical importance to extend the study to the whole extreme Kerr throat, not just the NHEK region. It is also essential to investigate the observational signatures of charged particles inside or outside the Kerr throat.

ACKNOWLEDGMENTS

We are very thankful to Qiaomu Peng and Haopeng Yan for helpful discussions. The work is partly supported by NSFC Grants No. 12275004, No. 12205013, and No. 11873044. M. G. is also endorsed by “the Fundamental Research Funds for the Central Universities” with Grant No. 2021NTST13.

APPENDIX: PROOF OF $C + L^2 \geq 0$ IN THE WALD POTENTIAL

In this section we demonstrate that the constraint $d = C + L^2 \geq 0$ holds for the motions in NHEK under the Wald potential Eq. (4.28). The angular potential takes

$$\Theta(z) = az^2 + bz + c \quad (\text{A1})$$

with

$$\begin{aligned} a &= 1 - (L + \mathfrak{B})^2/4, & b &= -C - 3L^2/2 + \mathfrak{B}^2/2, \\ c &= C + (L + \mathfrak{B})(3L - \mathfrak{B})/4 - 1. \end{aligned} \quad (\text{A2})$$

On one hand, for the oscillating motions, we have

$$d > C + L^2 - 1 \geq C + \frac{1}{4}(L + \mathfrak{B})(3L - \mathfrak{B}) - 1 = c \geq 0, \quad (\text{A3})$$

where we have used $(L + \mathfrak{B})(3L - \mathfrak{B}) \leq 4L^2$. So we have $d > 0$ for the oscillating motions. Then, for the vortical motions, the constraint is

$$a < 0, \quad c < 0, \quad 0 < b < -2a, \quad b^2 - 4ac > 0. \quad (\text{A4})$$

Define $x_{\pm} = L \pm \mathfrak{B}$, thus

$$a = 1 - \frac{1}{4}x_{\pm}^2, \quad b = \frac{1}{2}x_+x_- - d, \quad c = d - \frac{1}{4}x_+^2 - 1. \quad (\text{A5})$$

The expression of x_{\pm} can be written as

$$x_+ = \pm \frac{b + d}{\sqrt{1 - a}}, \quad x_- = \mp 2\sqrt{1 - a}. \quad (\text{A6})$$

Inserting Eq. (A6) into the third equation of Eq. (A5), we obtain

$$d^2 + Sd + \mathcal{T} = 0, \quad (\text{A7})$$

where

$$S = 2(b + 2a - 2), \quad \mathcal{T} = b^2 + 4(1 - a)(1 + c). \quad (\text{A8})$$

The roots of Eq. (A7) are

$$d_{\pm} = \frac{1}{2}(-S \pm \sqrt{S^2 - 3\mathcal{T}}). \quad (\text{A9})$$

Since $0 < b < -2a$, one has $S < -4$. Moreover, the inequality $4ac < b^2 < 4a^2$ means $a < c < 0$, thus we have

$$\mathcal{T} = b^2 - 4ac + 4(1 - a + c) > 4(1 - a + c) > 4 > 0. \quad (\text{A10})$$

Therefore, we have $|S| > \sqrt{S^2 - 4\mathcal{T}}$ and the roots must satisfy

$$d_+ > d_- > 0, \quad (\text{A11})$$

which means $d > 0$ for the vortical motions.

- [1] K. Akiyama *et al.* (Event Horizon Telescope Collaboration), First M87 event horizon telescope results. I. The shadow of the supermassive black hole, *Astrophys. J. Lett.* **875**, L1 (2019).
- [2] K. Akiyama *et al.* (Event Horizon Telescope Collaboration), First sagittarius A* event horizon telescope results. I. The shadow of the supermassive black hole in the center of the Milky Way, *Astrophys. J. Lett.* **930**, L12 (2022).
- [3] J. A. Rueda, R. Ruffini, and R. P. Kerr, Gravitomagnetic interaction of a kerr black hole with a magnetic field as the source of the jetted GeV radiation of gamma-ray bursts, *Astrophys. J.* **929**, 56 (2022).
- [4] K. Akiyama *et al.* (Event Horizon Telescope Collaboration), First M87 event horizon telescope results. VIII. Magnetic field structure near the event horizon, *Astrophys. J. Lett.* **910**, L13 (2021).
- [5] Z. Hu, Y. Hou, H. Yan, M. Guo, and B. Chen, Polarized images of synchrotron radiations in curved spacetime, *Eur. Phys. J. C* **82**, 1166 (2022).
- [6] H. Zhu and M. Guo, Polarized image of synchrotron radiations of hotspots in Schwarzschild-Melvin black hole spacetime, [arXiv:2205.04777](https://arxiv.org/abs/2205.04777).
- [7] T. Lee, Z. Hu, M. Guo, and B. Chen, Circular orbits and polarized images of charged particles orbiting Kerr black hole with a weak magnetic field, [arXiv:2211.04143](https://arxiv.org/abs/2211.04143).
- [8] K. Akiyama *et al.* (Event Horizon Telescope Collaboration), The polarized image of a synchrotron-emitting ring of gas orbiting a black hole, *Astrophys. J.* **912**, 35 (2021).
- [9] Z. Gelles, E. Himwich, D. C. M. Palumbo, and M. D. Johnson, Polarized image of equatorial emission in the Kerr geometry, *Phys. Rev. D* **104**, 044060 (2021).
- [10] X. Qin, S. Chen, Z. Zhang, and J. Jing, Polarized image of a rotating black hole in scalar–tensor–vector–gravity theory, *Astrophys. J.* **938**, 2 (2022).
- [11] X. Liu, S. Chen, and J. Jing, Polarization distribution in the image of a synchrotron emitting ring around a regular black hole, *Sci. China Phys. Mech. Astron.* **65**, 120411 (2022).
- [12] M. Dovciak, V. Karas, and G. Matt, Polarization signatures of strong gravity in AGN accretion discs, *Mon. Not. R. Astron. Soc.* **355**, 1005 (2004).
- [13] M. Y. Piotrovich, N. A. Silant’ev, Y. N. Gnedin, and T. M. Natsvlshvili, Magnetic fields of black holes and the variability plane, [arXiv:1002.4948](https://arxiv.org/abs/1002.4948).
- [14] R. A. Daly, Black hole spin and accretion disk magnetic field strength estimates for more than 750 AGN and multiple GBH, *Astrophys. J.* **886**, 37 (2019).
- [15] M. Zajaček, A. Tursunov, A. Eckart, and S. Britzen, On the charge of the Galactic centre black hole, *Mon. Not. R. Astron. Soc.* **480**, 4408 (2018).
- [16] M. Zajaček and A. Tursunov, Electric charge of black holes: Is it really always negligible?, [arXiv:1904.04654](https://arxiv.org/abs/1904.04654).
- [17] A. R. Prasanna and C. V. Vishveshwara, Charged particle motion in an electromagnetic field on Kerr background geometry, *Pramana* **11**, 359 (1978).
- [18] A. N. Aliev and N. Ozdemir, Motion of charged particles around a rotating black hole in a magnetic field, *Mon. Not. R. Astron. Soc.* **336**, 241 (2002).
- [19] V. P. Frolov and A. A. Shoom, Motion of charged particles near weakly magnetized Schwarzschild black hole, *Phys. Rev. D* **82**, 084034 (2010).
- [20] A. Abdujabbarov and B. Ahmedov, Charged particle motion around rotating black hole in braneworld immersed in magnetic field, *Phys. Rev. D* **81**, 044022 (2010).
- [21] S. Hussain, I. Hussain, and M. Jamil, Dynamics of a charged particle around a slowly rotating Kerr black hole immersed in magnetic field, *Eur. Phys. J. C* **74**, 3210 (2014).
- [22] S. Shaymatov, B. Narzilloev, A. Abdujabbarov, and C. Bambi, Charged particle motion around a magnetized Reissner-Nordström black hole, *Phys. Rev. D* **103**, 124066 (2021).
- [23] A. M. A. Zahrani, Charged particle circular orbits around weakly charged and magnetized kerr black holes, *Astrophys. J.* **937**, 50 (2022).
- [24] B. Carter, Global structure of the Kerr family of gravitational fields, *Phys. Rev.* **174**, 1559 (1968).
- [25] D. Pugliese, H. Quevedo, and R. Ruffini, Motion of charged test particles in Reissner-Nordström spacetime, *Phys. Rev. D* **83**, 104052 (2011).
- [26] E. Hackmann and H. Xu, Charged particle motion in Kerr-Newmann space-times, *Phys. Rev. D* **87**, 124030 (2013).
- [27] J. Kovar, Z. Stuchlík, and V. Karas, Off-equatorial orbits in strong gravitational fields near compact objects, *Classical Quantum Gravity* **25**, 095011 (2008).
- [28] J. Kovar, O. Kopacek, V. Karas, and Z. Stuchlík, Off-equatorial orbits in strong gravitational fields near compact objects—II: Halo motion around magnetic compact stars and magnetized black holes, *Classical Quantum Gravity* **27**, 135006 (2010).
- [29] R. Shiose, M. Kimura, and T. Chiba, Motion of charged particles around a weakly magnetized rotating black hole, *Phys. Rev. D* **90**, 124016 (2014).
- [30] A. Tursunov, Z. Stuchlík, and M. Kološ, Circular orbits and related quasiharmonic oscillatory motion of charged particles around weakly magnetized rotating black holes, *Phys. Rev. D* **93**, 084012 (2016).
- [31] M. Takahashi and H. Koyama, Chaotic motion of charged particles in an electromagnetic field surrounding a rotating black hole, *Astrophys. J.* **693**, 472 (2009).
- [32] O. Kopacek, J. Kovar, V. Karas, and Z. Stuchlík, Recurrence plots and chaotic motion around Kerr black hole, *AIP Conf. Proc.* **1283**, 278 (2010).
- [33] Z. Stuchlík and M. Kološ, Acceleration of the charged particles due to chaotic scattering in the combined black hole gravitational field and asymptotically uniform magnetic field, *Eur. Phys. J. C* **76**, 32 (2016).
- [34] C.-Y. Liu, Chaotic motion of charged particles around a weakly magnetized Kerr-Newman black hole, [arXiv:1806.09993](https://arxiv.org/abs/1806.09993).
- [35] X. Sun, X. Wu, Y. Wang, C. Deng, B. Liu, and E. Liang, Dynamics of charged particles moving around Kerr black hole with inductive charge and external magnetic field, *Universe* **7**, 410 (2021).
- [36] J. M. Bardeen and G. T. Horowitz, The extreme Kerr throat geometry: A vacuum analog of $AdS_2 \times S^2$, *Phys. Rev. D* **60**, 104030 (1999).
- [37] M. Guica, T. Hartman, W. Song, and A. Strominger, The Kerr/CFT correspondence, *Phys. Rev. D* **80**, 124008 (2009).

- [38] I. Bredberg, T. Hartman, W. Song, and A. Strominger, Black hole superradiance from Kerr/CFT, *J. High Energy Phys.* **04** (2010) 019.
- [39] B. Chen, J. Long, and J.-j. Zhang, Hidden conformal symmetry of extremal black holes, *Phys. Rev. D* **82**, 104017 (2010).
- [40] D. Kapec and A. Lupsasca, Particle motion near high-spin black holes, *Classical Quantum Gravity* **37**, 015006 (2020).
- [41] G. Compère and A. Druart, Near-horizon geodesics of high-spin black holes, *Phys. Rev. D* **101**, 084042 (2020).
- [42] A. Galajinsky, Particle dynamics near extreme Kerr throat and supersymmetry, *J. High Energy Phys.* **11** (2010) 126.
- [43] A. Galajinsky and K. Orekhov, $N = 2$ superparticle near horizon of extreme Kerr-Newman-AdS-dS black hole, *Nucl. Phys.* **B850**, 339 (2011).
- [44] J. E. McClintock, R. Shafee, R. Narayan, R. A. Remillard, S. W. Davis, and L.-X. Li, The spin of the near-extreme Kerr black hole GRS 1915 + 105, *Astrophys. J.* **652**, 518 (2006).
- [45] L. Gou, J. E. McClintock, R. A. Remillard, J. F. Steiner, M. J. Reid, J. A. Orosz, R. Narayan, M. Hanke, and J. García, Confirmation via the continuum-fitting method that the spin of the black hole in Cygnus X-1 is extreme, *Astrophys. J.* **790**, 29 (2014).
- [46] D. Grumiller and A.-M. Pison, Exact relativistic viscous fluid solutions in near horizon extremal Kerr background, *arXiv:0909.2041*.
- [47] A. M. Al Zahrani, V. P. Frolov, and A. A. Shoom, Particle dynamics in weakly charged extreme Kerr throat, *Int. J. Mod. Phys. D* **20**, 649 (2011).
- [48] G. Compère and R. Oliveri, Near-horizon extreme Kerr magnetospheres, *Phys. Rev. D* **93**, 024035 (2016).
- [49] S. E. Gralla, A. Lupsasca, and A. Strominger, Near-horizon Kerr magnetosphere, *Phys. Rev. D* **93**, 104041 (2016).
- [50] F. Camilloni, G. Grignani, T. Harmark, R. Oliveri, and M. Orselli, Force-free magnetosphere attractors for near-horizon extreme and near-extreme limits of Kerr black hole, *Classical Quantum Gravity* **38**, 075022 (2021).
- [51] F. Camilloni, G. Grignani, T. Harmark, R. Oliveri, and M. Orselli, Moving away from the near-horizon attractor of the extreme Kerr force-free magnetosphere, *J. Cosmol. Astropart. Phys.* **10** (2020) 048.
- [52] A. P. Porfyriadis, Y. Shi, and A. Strominger, Photon emission near extreme Kerr black holes, *Phys. Rev. D* **95**, 064009 (2017).
- [53] G. Compère and R. Oliveri, Self-similar accretion in thin discs around near-extremal black holes, *Mon. Not. R. Astron. Soc.* **468**, 4351 (2017).
- [54] S. E. Gralla, A. Lupsasca, and A. Strominger, Observational signature of high spin at the event horizon telescope, *Mon. Not. R. Astron. Soc.* **475**, 3829 (2018).
- [55] M. Guo, N. A. Obers, and H. Yan, Observational signatures of near-extremal Kerr-like black holes in a modified gravity theory at the event horizon telescope, *Phys. Rev. D* **98**, 084063 (2018).
- [56] M. Guo, S. Song, and H. Yan, Observational signature of a near-extremal Kerr-Sen black hole in the heterotic string theory, *Phys. Rev. D* **101**, 024055 (2020).
- [57] P.-C. Li, M. Guo, and B. Chen, High spin expansion for null geodesics, *Classical Quantum Gravity* **38**, 065008 (2021).
- [58] H. Yan, Z. Hu, M. Guo, and B. Chen, Photon emissions from near-horizon extremal and near-extremal Kerr equatorial emitters, *Phys. Rev. D* **104**, 124005 (2021).
- [59] H. Yan, Influence of a plasma on the observational signature of a high-spin Kerr black hole, *Phys. Rev. D* **99**, 084050 (2019).
- [60] R. M. Wald, Black hole in a uniform magnetic field, *Phys. Rev. D* **10**, 1680 (1974).
- [61] B. S. Kay and R. M. Wald, Theorems on the uniqueness and thermal properties of stationary, nonsingular, quasifree states on space-times with a bifurcate killing horizon, *Phys. Rep.* **207**, 49 (1991).
- [62] A. Chamblin, R. Emparan, and G. W. Gibbons, Superconducting p-branes and extremal black holes, *Phys. Rev. D* **58**, 084009 (1998).
- [63] R. Ruffini and J. R. Wilson, Relativistic magnetohydrodynamical effects of plasma accreting into a black hole, *Phys. Rev. D* **12**, 2959 (1975).
- [64] R. D. Blandford and R. L. Znajek, Electromagnetic extraction of energy from Kerr black holes, *Mon. Not. R. Astron. Soc.* **179**, 433 (1977).
- [65] J. Bičák and F. Hejda, Near-horizon description of extremal magnetized stationary black holes and Meissner effect, *Phys. Rev. D* **92**, 104006 (2015).